surface of the target material. They found that the particle-particle collision efficiency decreases from the stagnation point in the middle of the material beneath the jet to the maximum depth on the W-shaped scar. This decreases the "screening" effect of particles on the surface and increases the erosion rate.

Clark [34] provided an excellent summary on the effects of fluid flow field on various parameters like velocity, impact angle, particle concentration, particle size, viscosity and target shape. More recently, Gustavsson [35] developed an erosion model using the Eulerian fluid modelling and incorporated cutting and deformation wear. An important element to this model is the shearing and normal viscous dissipation term to describe the contribution of ductile and brittle erosion respectively. In view of the advancement of Computational Fluid Dynamics (CFD), it is believed that the difficulty of solving complex multiphase equations of fluid motion and tracking particle trajectory will improve erosion prediction models.

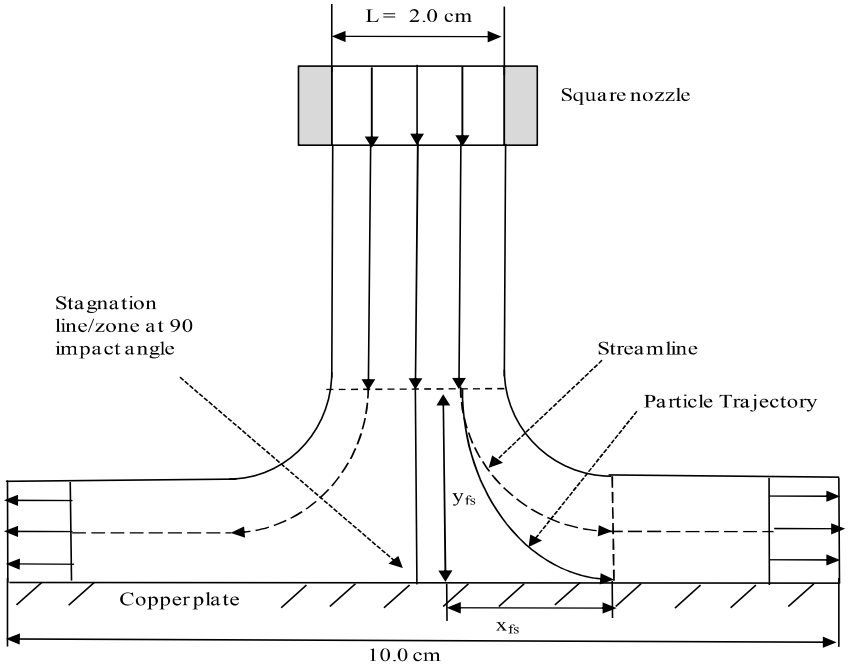

Figure 2.12 Two phase flow of particles impinging on a metallic flat plate [16]

2.1.3 Erosion models

Many researchers have developed predictive models in order to quantify the material loss during erosion. Meng and Ludema [36] surveyed 5466 papers and found that there were more than 182 equations for many types of wear. From these 182 equations, 28 models were chosen based on a list of criteria [36]. After studying the equations, they found that a total of

33 different parameters were quoted in different models and each equation had an average of 5 parameters. This paper highlighted some of the problems with the current state of wear modelling, together with suggestions to improve them. One of the suggestions given was for researchers to clearly attach full documentation, assumptions, limitations and critiques of models, so that other researchers can either build on this work or find alternatives to overcome limitations. This section will discuss selected erosion models and their underlying mechanisms and theories, based on which they were derived.

2.1.3.1 Finnie's erosion model

Finnie [2] first developed an erosion model in which he stated that the wear of a surface due to solid particle erosion would be dependent on the particle motion entrained in the flowing fluid and the interaction between the particles and the surface. He developed his model by solving the equation of motion of a particle, assuming material removal caused by the particle follows a certain path along the surface of the material. In this model, the volume of the material removed is the result of the area swept by the particle tip and the width of the cutting surface. Eq. (2.2) assumes the particle tip leaves the surface while cutting, while Eq. (2.3) applies to higher angles where the horizontal motion of the particle ceases while cutting. It allows accurate prediction of the volume of material removed at low impact angles but underestimates erosion at high angles, more significantly its failure to predict erosion at 90°. This approach was recognised as unsuitable for brittle material where phenomenon like fracture and crack propagation occur. Finnie's comprehensive analysis and model formed the foundation for other researchers in the field to develop erosion models.

$$V_r = \frac{mv^2}{p\Psi K}\left(\sin\alpha - \frac{6}{K}\sin^2\alpha\right) \qquad \text{if } \tan\alpha \le \frac{K}{6} \qquad (2.2)$$

$$V_r = \frac{mv^2}{p\Psi K}\left(\frac{K\cos^2\alpha}{6}\right) \qquad \text{if } \tan\alpha \ge \frac{K}{6} \qquad (2.3)$$

where K is the ratio of the vertical force component on the particle face to the horizontal force component, p is the plastic flow stress, Ψ is the ratio of the depth of contact to the depth of cut, α is the angle of particle impact, m is the mass of abrasive particle, v is the particle velocity and V_r is the volume of material removed from the surface.

2.1.3.2 Bitter's erosion model

Bitter [3, 4] in his model highlighted that there are two types of wear that occur during erosion. One is the repeated deformation during particle impingement which causes the material to break loose, and the other is caused by the cutting action of free moving particles. He formulated his model based on the mass, velocity and impacting angles of the particle combined with the mechanical and physical properties of the particles and target material. Bitter treated the model of deformation wear and cutting wear separately in terms of its derivation. In his deformation model (Eq. (2.4)), he used the energy balance approach by assuming that the energy absorbed during collision of the particles in the surface layer causes deformation wear. For his cutting model expressed by Eq. (2.5) and (2.6), similar to Finnie, he considered two scenarios of cutting when the particle leaves the surface with a horizontal velocity component or a second scenario where the horizontal velocity component becomes zero during collision. The difference in which he treats his cutting model compared to Finnie's model lies in the fact that unlike Finnie who assumes the material strength determines the energy absorption during cutting, Bitter relates the energy absorption (elastic and elastic-plastic) to the integrated product of the stress-strain curve. Another assumption made by Finnie is that surface roughness is proportional to the angle of attack, assuming the surface becomes rough during erosion. Tests done at the Shell lab showed that surface roughness is a function of mechanical properties, particle size, particle shape and impact angle [3,4]. So the surface roughness must be caused by some other factor which he attributed to the repeated deformation of particles at higher angles. Taking this into account, his model gave a good approximation of erosion even at high angles, which Finnie's model did not manage to predict accurately.

$$W_D = \frac{1}{2}\frac{m\left(v\sin\alpha - U_p\right)^2}{\gamma} \tag{2.4}$$

$$W_{c1} = 2mC_1\left(\frac{v\sin\alpha - U_p^2}{\sqrt{v\sin\alpha}}\right)\left[v\cos\alpha - C_1\frac{v\sin\alpha - U_p^2}{\sqrt{v\sin\alpha}}\rho_1\right] \tag{2.5}$$

$$W_{c2} = \frac{1}{2}\left[\frac{mv^2\cos^2\alpha - k_1\left(v\sin\alpha - U_p\right)^{3/2}}{\rho_1}\right] \tag{2.6}$$

where m is the total mass of impinging particles, W_D is the total deformation wear, C_1 is a constant dependent on density and elastic load limit, W_{c1} is the cutting wear unit volume loss when the horizontal velocity component $v \neq 0$ when it leaves the body surface, W_{c2} is the cutting wear unit volume loss when the horizontal velocity component = 0 during collision, α is the impact angle, ρ_1 is the energy needed to scratch out a unit volume from surface or cutting wear factor, U_p is the maximum particle velocity at which the collision is purely elastic, γ is the energy needed to remove a unit volume of material from the body by deformation wear or the deformation wear factor and k_1 is the constant based on mechanical properties.

2.1.3.3 Hashish's erosion model

Hashish [12] expanded Finnie's model to overcome deficiencies in some of the experimental observations such as higher velocity exponents ($n > 2$) as described in section 2.1.2.1. Other factors that were taken into account were the particle shape and density, see Eq. (2.7). In Finnie's model, he assumed that the width of the cut does not vary in a two dimensional analysis, and this was considered in Hashish's model. Hashish introduced a characteristic velocity C_K expressed by Eq. (2.8) which combines particle and material characteristics including material flow stress, particle density and particle shape factor. He also took into account Bitter's equation for deformation wear, which included a threshold velocity which defined an angle below which only elastic deformation would occur. However, he applied flow stress as the material property used to remove a unit volume by deformation wear. This was deemed as a good approximation of the amount of stress required to deform the material. The effect of hydrodynamic loading was included in his analysis but he found it to have a small effect compared to material resistance.

$$E = \frac{14}{\pi}\frac{\rho_m}{\rho_p}\left(\frac{v\sin\alpha - v_c}{C_k}\right)^{2.5}\cot\alpha \tag{2.7}$$

$$C_k = \sqrt{\frac{3\sigma_s R_f^{3/5}}{\rho_p}} = \frac{V_k}{R_f^{1.2}} \tag{2.8}$$

where E is the ratio of the mass of material removed to the mass of abrasive particle, C_K is the modified characteristic velocity that combines material and particle characteristics,

σ_s is the material flow stress, R_f is the particle roundness, ρ_m is the density of the target material and ρ_p is the density of the particle.

2.1.3.4 Hutchings's erosion model

Hutchings [1] developed two models for erosion at low impact angles and high impact angles as shown in Eq. (2.9) and (2.10) respectively. These models assume that the problem can be analysed quasi-statically and ignore the effect of strain rate sensitivity of the material. In Eq. (2.9), it is assumed that the particle indents the material and forms a rim of plastically deformed material around the indentation which is removed as wear debris. This is schematically illustrated in Figure 2.13. As the particle indents the target material at a constant indentation pressure (hardness), it will come to rest at a certain depth at which the work done is assumed to be equal to the initial kinetic energy of the particle. Each impact would displace the material from the indentation formed. However, it would only be removed as wear debris once it has undergone several cycles of plastic deformation or has become severely work hardened. The efficiency of material removal K, in this process is typically between 5 x 10^{-3} and 10^{-1} [1]. The velocity exponent n is about 2 and is also a function of the impact angle, θ.

The model given in Eq. (2.9) is suitable for wear modes at shallow impact angles where cutting action occurs. At higher impact angles or for spherical particles, the cutting mechanism does not occur. Hutchings [1] modelled it by two ways. In the first case, he assumed that the material becomes detached when the accumulated plastic strain reaches a critical value, and in the second case he assumed that the problem could be treated as low-cycle fatigue. In both cases he reached the same conclusion and modelled it in Eq. (2.10). The fundamental difference between this model and the model for cutting is the higher velocity exponent of 3 presented in this model and the fact that the new parameter ε_c which is the critical strain to failure is introduced. He cautioned that erosion occurs on heavily strain-hardened material at very short time scales, which leads to extremely high strain rates [37]. For normal impacts of sphere on a rigid-plastic surface, the mean strain can be modelled through Eq. (2.11). Strain rates up to 10^6 s^{-1} are experienced during erosion processes. Figure 2.14 shows the mean plastic strain rate predicted by Eq. (2.11) for different velocities and particle radii inputs [37]. Higher strain rates are seen for smaller particles as the impact duration is shorter for smaller particles compared to larger particles.

$$E_m = \frac{K_1 \rho_m v^n}{H_s} \alpha \tag{2.9}$$

$$E_m = \frac{K_2 \rho_m \rho_s^{1/2} v^3}{\varepsilon_c^2 H_S^{3/2}} \tag{2.10}$$

$$\dot{\varepsilon} = \frac{2^{3/2} v^{1/2}}{5\pi r_p} \left(\frac{3H_s}{2\rho_s} \right)^{1/4} \tag{2.11}$$

where H_s is the hardness of the target material, K_1 & K_2 are the fraction of the material displaced from the indentation as wear debris, ρ_m is the density of material being eroded, ρ_s is the density of spherical particles, ε_c is the critical plastic strain where detachment of wear particles occur, $\dot{\varepsilon}$ is the mean plastic strain rate, r_p is the radius of the spherical particle and E_m is the ratio of mass of material removed over mass of erosive particles striking the surface.

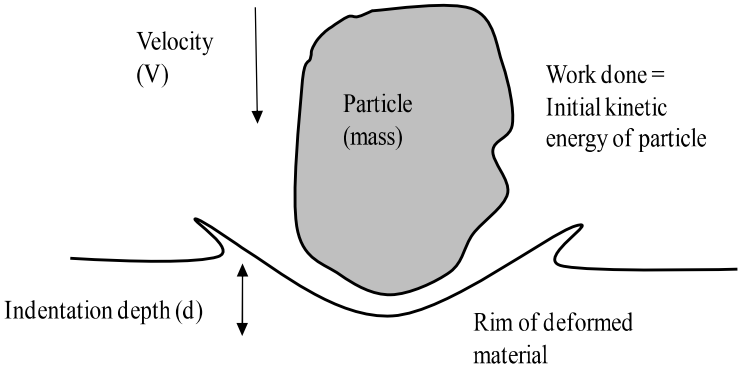

Figure 2.13 Schematic showing the rim of plastically deformed material around an indentation crater and derivation of Eq. (2.9) [1].

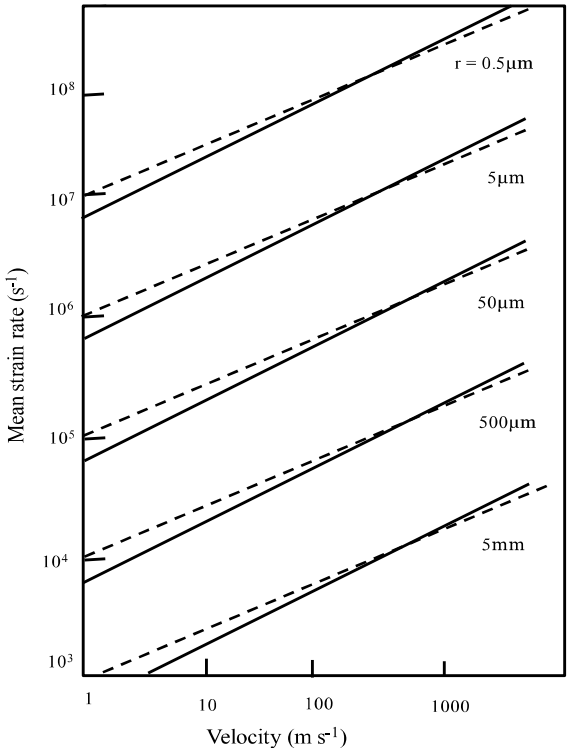

Figure 2.14 Mean strain estimated by Eq. (2. 11) for impact of steel spheres of varying radii on to a steel surface. Solid lines – purely elastic behaviour, broken lines – perfectly plastic behaviour [37].

Bahadur [38] in a review on the structure of erosive models, stated that it is not surprising that there exists inadequacies in erosion prediction models, considering the multiplicity of variables involved and the dynamic interaction between the particle and target materials. He listed some of the complications in modelling erosion as given in Table 2.2.

Table 2.2 Complexity in modelling erosion [38]

Parameter	**Complexity**
Strain rate	High strain rate deformation - a function of impact velocity, particle geometry, target material characteristics.
Temperature	Localised temperature rise – a function of the particle mass, velocity and concentration of the fluid stream, coefficient of restitution, indentation and thermal characteristics of the target material.
Particle interaction	• Inter-collision between the incoming and reflected particles. • Particle fragmentation • Embedment of particles on the impacting surface
Target material	• Work hardening and annealing effects • Change in impingement angle due to crater formation. • Measuring hardness and ductility under dynamic conditions

2.2 Corrosion

2.2.1 Fundamentals of corrosion mechanisms

Corrosion is defined as the degradation of a metal when it undergoes an electrochemical reaction with the environment [39-44]. This phenomenon has a potential to cause catastrophic failures to materials if the causes and prevention of corrosion are not well understood. There are many types of corrosion that can occur in the environment namely uniform, pitting, crevice, galvanic, intergranular and flow-induced. This section of the literature review will focus mainly on the general principles of corrosion and flow corrosion.

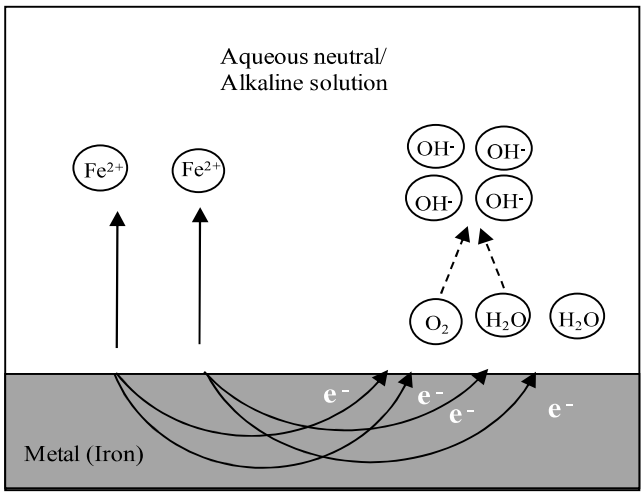

Figure 2.15 Schematic diagram showing the electrochemical process that occurs during corrosion

The schematic diagram shown in Figure 2.15 describes a simple electrochemical reaction that occurs during corrosion. For corrosion to take place, a few essential elements have to be present to allow electrochemical reaction to occur. These elements are an anode, a cathode, an electrolyte and some form of connection between the anodic region and the cathodic region. The anode and cathode do not have to be from two separate metals, it could be from different regions of the same metal. Assuming the anodic and cathodic regions are from the same metal, we shall consider the reaction that occurs in Figure 2.15 using iron as the metal and an aqueous neutral or alkaline solution as the electrolyte.

Anodic reaction (Oxidation reaction) $Fe \rightarrow Fe^{2+} + 2e^{-}$ (2.12)

Cathodic reaction (Reduction reaction) $O_2 + 2H_2O + 4e^{-} \rightarrow 4OH^{-}$ (2.13)

Overall reaction $Fe + O_2 + 2H_2O \xrightarrow{4e^{-}} Fe^{2+} + 4OH^{-}$ (2.14)

When the anodic region of the iron is oxidised into ions, it produces electrons (Eq. (2.12)). These electrons are consumed at the cathodic region, where the reduction cathodic reaction occurs as shown in Eq. (2.13). The overall reaction is shown in Eq. (2.14). These equations reflect the simplest form of electrochemical reaction that takes place during corrosion.

2.2.1.1 Passivity

Passivity is when a metal susceptible to corrosion, experiences a lower corrosion rate in a given environmental condition [44]. The reason for passivity is attributed to a passive layer that is formed on the metal surface protecting it from corrosion. The passive film is formed through the reaction of the metal with the environment and usually forms metal oxides that prevent charge transfer across the metal surface, hence preventing chemical reactions. The passive film is important as it reduces the corrosion rate. Typically, the thickness of a passive film is between 1 and 10 nm [45]. Passivation is the terminology used to describe the transition from an active state to a passive state. Due to the presence of a passive film, the dissolution rate of the passive metal is lower than an active metal at a given potential. The ideal polarization curve of a passivating metal can be divided into three potential regions as follows [45]:

- the active region
- the passive region
- the transpassive region

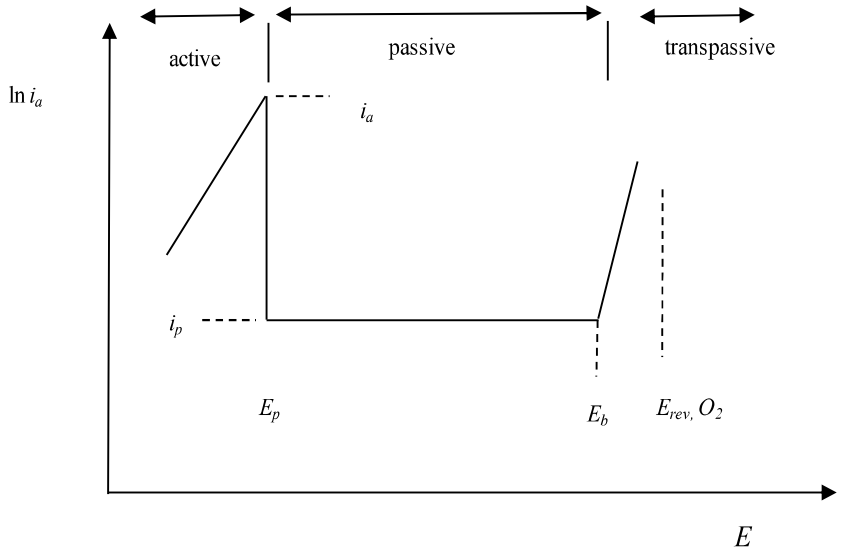

Figure 2.16 Variation of partial anodic current density with passivating metal potential [45]

Figure 2.16 shows the variation of anodic partial current density with respect to a given applied potential [45]. The passivation potential E_p clearly distinguishes the region between the active potential and the passive potential. The passive current density i_p provides information on the dissolution rate of the metal in the passive potential region, while the current density at the maximum of the passivation potential is the passivation current density i_a. The transpassivation potential E_b distinguishes the region between passive and transpassive behaviour. From the graph, it is observed that beyond the transpassive region, the anodic partial current density increases rapidly with increasing potential. The reason for this may be due to uniform transpassive dissolution caused by passive film oxidation, pitting occurrence or oxygen evolution [45].

The passive film however, can also breakdown electrochemically, chemically and mechanically [44]. In the context of this thesis, we shall consider mechanical breakdown due to solid particle erosion as the dominant mechanism. Figure 2.17 shows the experimental results obtained by Sasaki and Burstein [46] that depicts the linear trend between impact energy and mean peak current. They also noticed that there was a minimum impact energy below which there was no current transient and suggested that below a certain threshold, the impact would only cause elastic deformation and no plastic flow. This threshold also depends on the impact angle of the particle, where there exists a sharp current cut-off at 0.03 μJ for a 90° impact angle and 0.037 μJ for 50°. Below these impact energies, there is no anodic current transient observed.

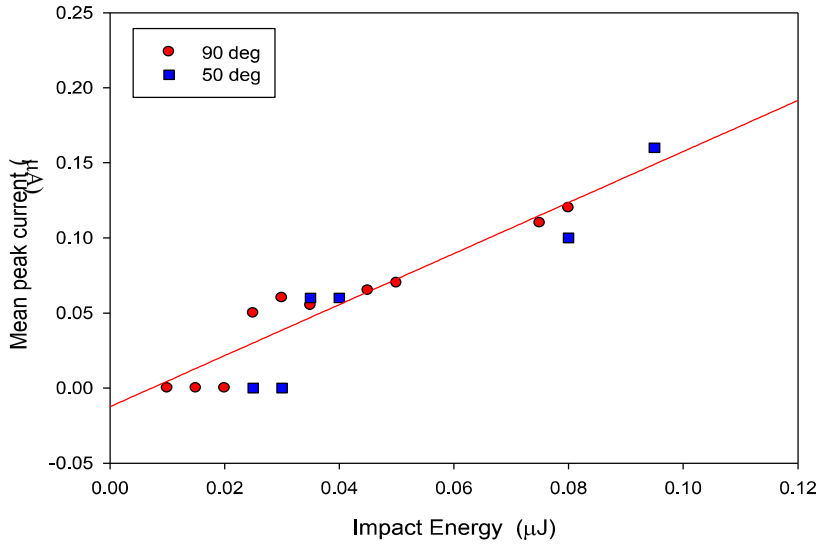

Figure 2.17 Experimental results depicting the linear trend between impact energy and mean peak current observed by Sasaki and Burstein [46]

~~Conditions of passivity, immunity and corrosion can also be shown using a Pourbaix diagram. The Pourbaix diagram illustrates the relationship between the potential and pH and its influence on the stability of different species [39]. A typical Pourbaix diagram for iron (Fe) is shown in Figure 2.18 [39]. The diagram is divided into three main regions of corrosion, immunity and passivity which vary with pH and applied potential. A general trend is seen where a metal at low pH (acidic conditions) and high negative potentials is seen to be in an immunity state, while at low pH and more positive potentials, the metal is seen to be in a corrosion state. A metal is in a passive state at high pH and positive potentials (alkaline conditions). Figure 2.18 also shows the stability of the species such as Fe, Fe^{2+}, Fe^{3+} $_{(aq)}$, $FeO_2^-{}_{(aq)}$, $FeO_2H_{(aq)}$ is in the three different states. This diagram serves to illustrate that depending on the solution pH and the applied potential, the metal iron can be in various states and is an important environmental consideration in corrosion studies.~~

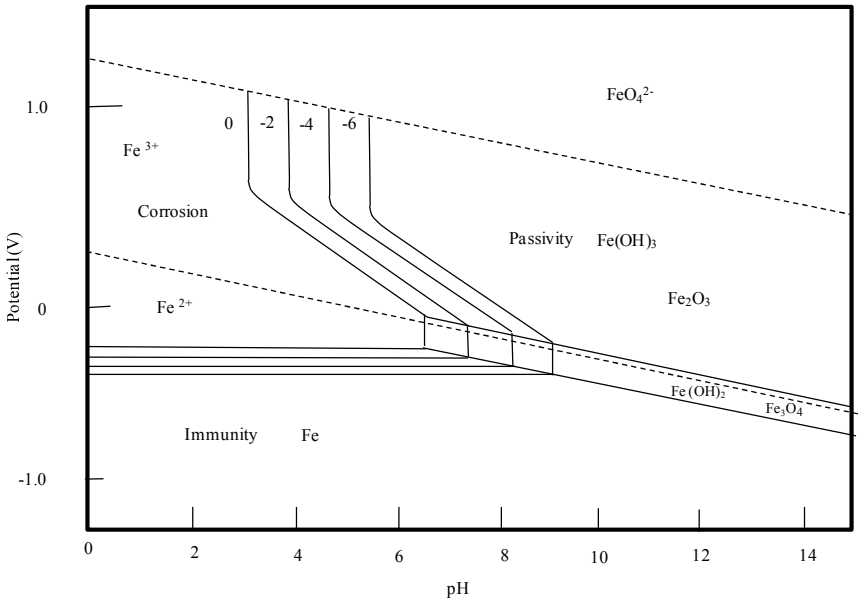

Figure 2.18 ~~Pourbaix diagram for iron (Fe) showing regions of corrosion, passivation and immunity~~

2.2.2 Flow corrosion

Flow corrosion occurs when a metal is exposed to a flowing corrosive fluid and the corrosion rate is accelerated by the motion of the flowing fluid [43]. Heitz [47] identified four types of flow induced corrosion, namely mass transport controlled, phase transport controlled, erosion-corrosion and cavitation. Figure 2.19 illustrates the four types of flow induced corrosion. This section of the literature review will discuss mainly on mass transport controlled corrosion. Heitz [47] described the mass transfer process as convective diffusion where there is convection in the bulk solution and diffusion on the surface of the material. He highlighted some of the important fluid mechanics parameters, which are highlighted below, to understand the nature of flow corrosion.

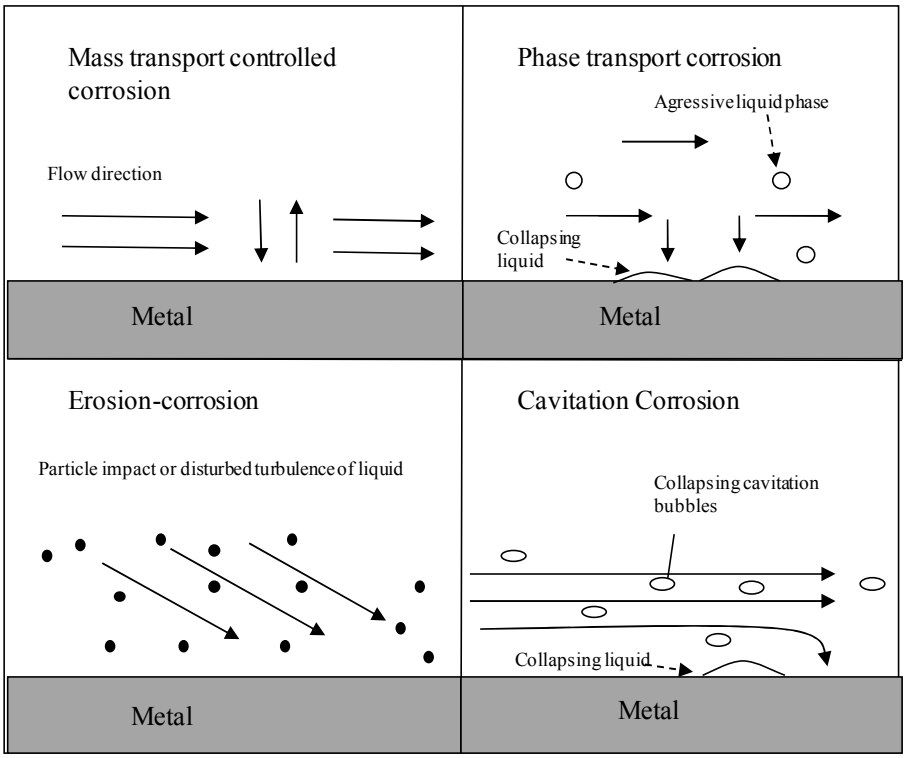

Figure 2.19 Types of flow induced corrosion [47]

Reynolds number, Re_p is the ratio of inertial forces of the fluid divided by the viscous force. This dimensionless number provides information on the type of flow whether it is laminar, turbulent or transitional. It could possibly be described as one of the most important dimensionless number in fluid mechanics [48]. Reynolds number can be expressed by Eq. (2.15):

$$Re_p = \frac{Vd}{\nu_k} \tag{2.15}$$

where V is the fluid velocity, d is the characteristic length dimension and ν_k is the kinematic viscosity. Schmidt number *Sc,* which is given by Eq. (2.16) is another dimensionless number defined as the ratio of momentum transfer to the mass transfer due to molecular diffusivity.

$$S_C = \frac{\nu_k}{D} \tag{2.16}$$

where D is the diffusion coefficient. Sherwood number *Sh,* represents the ratio of total mass transport of the fluid divided by the mass transport due to molecular diffusion in the fluid, and can be used to obtain the mass transfer coefficient as shown in Eq.(2.17). The relationship between the Sherwood number, Reynolds number and the Schmidt number is given by Eq. (2.18):

$$Sh = \frac{k_m d}{D} \tag{2.17}$$

and

$$Sh = a\, Re_p^b\, Sc^c \tag{2.18}$$

where *a, b, c* are constants. The mass transfer coefficient can also be derived from Eq. (2.19) where the rate of reaction, *J,* is a product of the mass transfer coefficient k_m and the concentration gradient ΔC_g.

$$J = k_m \Delta C_g \tag{2.19}$$

Other parameters that are also considered important in flow corrosion are the fluid velocity itself, *V* and the wall shear stress τ_w which is a direct measure of the viscous energy loss within the boundary layer.

$$\tau_w = \mu \frac{du}{dy} \tag{2.20}$$

where μ is the dynamic viscosity of fluid, and $\frac{du}{dy}$ is the velocity gradient at the wall. Wall shear stress is another parameter that affects the removal of the passive film due to the force exerted by the fluid on the surface of the metal that may cause removal of the corrosion products [49]. This section will review the flow corrosion hydrodynamic relationships of a jet impingement rig, as the relationships for a slurry pot erosion tester have not been well established. Effird [50] suggested that the mass transfer coefficient and the wall shear stress can be related using the Chilton Colburn analogy through Eq. (2.21):

$$k_m = 17.24\left(\frac{\tau}{\rho_f}\right)^{0.5} Sc^{2/3} \quad Sc > 100 \tag{2.21}$$

where ρ_f is the density of the fluid. He used a jet impingement rig to obtain a relationship between the wall shear stress and jet flow rate from the ferricyanide reduction experimental data. The relationship is shown in Eq. (2.22):

$$\tau_w = 852 Q_r^{1.8} \tag{2.22}$$

where Q_r is the flow rate in *l*/min. A correction factor was also given to correct the wall shear stress for other test fluids. Previously, Effird *et al*. [51] had tried to correlate steel corrosion in a pipe flow by using a jet impingement rig and a rotating cylinder. The jet impingement rig used to measure flow accelerated corrosion has a stagnation zone in the middle and its velocity component varies from the axial point to the radial point on the plate. Figure 2.20 shows the hydrodynamic characteristics of jet impingement on a flat plate showing four characteristic flow regions [51]. Region A is the laminar stagnation zone, region B is the high turbulence transition zone, region C is the low turbulence wall jet zone, region D is the hydrodynamic boundary layer. Symbols r_j, U_0 and H are the jet radius, jet velocity and jet nozzle to plate height respectively. The rotating cylinder on the other hand, has an advantage that transition from laminar flow to turbulent flow can occur at low rotation speeds. The results from their tests showed that the rate of corrosion increases as the wall shear stress increases in both rigs. The relationship between shear stress and corrosion rate is generally given by:

$$R_{corr} = a \tau_w^{\ b} \tag{2.23}$$

where R_{corr} is the steel corrosion rate and a and b are constants. Values of a = 7.7, 6.8 and 2.8 were obtained for pipe flow, jet impingement and rotating cylinder respectively. Values for the constant b were evaluated to be between 0.095 and 0.103 for each system. The lower values for the rotating cylinder were believed to be due to the drag coefficient data, which had significant turbulent shear forces and did not interact with the cylinder surface in a way to influence corrosion.

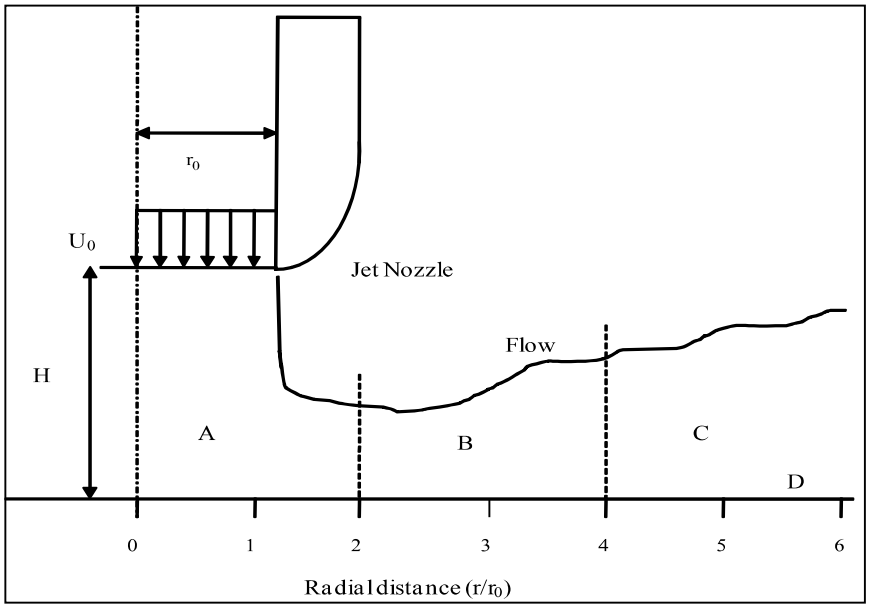

Figure 2.20 Hydrodynamic characteristics of jet impingement on a flat plate showing four characteristic flow regions [51].

Rao and Trass [52] found that the mass transfer coefficient could be obtained using the Sherwood number through the following relationships:

$$Sh = 0.046\, Re^{1.06}\left(\frac{a_n}{d_1}\right)^{-0.09} \qquad \text{for } \frac{a_n}{d_1} < 6.5 \qquad (2.24)$$

and

$$Sh = 0.107\, Re^{1.06}\left(\frac{a_n}{d_1}\right)^{-0.54} \qquad \text{for } \frac{a_n}{d_1} \geq 6.5 \qquad (2.25)$$

where a_n is the nozzle tip to plate stand-off distance and d_1 is the nozzle diameter. The development of two separate equations for $\frac{a_n}{d_1}$ above and below 6.5 was because below 6.5, the jet is still in a transition region and only above this did the jet exhibit a fully developed profile. Their data showed similarity with heat transfer studies in the wall jet region, except at the stagnation region where the erosion factor was observed to give a difference in Reynolds number dependency for heat transfer coefficients and mass transfer coefficients. In

a radial wall jet experiment conducted by Dawson and Trass [53], the following expression was obtained for Sherwood number:

$$Sh = 0.029\,Re^{0.93}\left(\frac{x_1}{d_2}\right)^{-1.0} \qquad Sc^{0.25} \quad for\ Sc \geq 100 \qquad (2.26)$$

x_1 is the radial distance from the stagnation point and d_2 is the jet diameter. Their results showed good correlation with their predicted theory at low Schmidt numbers but discrepancies were observed at high Schmidt numbers. A couple of causes were provided to explain this phenomenon. It was proposed that mechanical erosion of the surface may contribute to the total mass transfer and surface roughening altering the convective transfer.

Poulson [49] has however argued that wall shear stress may not contribute to the removal of corrosion products. According to him, it is difficult to measure the wall shear stress and there is no evidence that it removes the corrosion products. It has been well established that mass transfer has an effect on flow corrosion. However, more studies need to be done to determine whether wall shear stress has any contribution to flow corrosion.

2.3 Erosion – corrosion

2.3.1 Introduction

In previous sections, the topic of erosion and corrosion were reviewed separately. In this section, the combined action of erosion and corrosion, termed erosion-corrosion will be reviewed. Only solid particle erosion-corrosion will be considered within the scope of this work. Erosion-corrosion can be described as the wear caused by the combined action of the mechanical process of solid particle erosion and the electrochemical process of corrosion. This phenomenon is a common occurrence in the oil and gas industry, mining industry, chemical plants, power plants and desalination plants where it causes damage to the fluid handling equipment such as pumps, impellers, valves and turbines. This may lead to the need of repair or replacement of these equipments which incurs high costs to these industries.

2.3.2 Synergy/Antagonism

Synergy is described as the additional wear rate experienced by a metal, which is higher than the sum of wear rates due to pure erosion and flow corrosion. Synergy of a material can be expressed by Eq. (2.27) and (2.28) [54, 55]:

$$T = E + C + S \tag{2.27}$$

$$S = T - (E + C) \tag{2.28}$$

where T is the total wear rate due to erosion-corrosion, E is the wear rate due to pure erosion, C is the wear rate due to flow corrosion and S is the additional wear rate due to synergistic effects. Synergy is said to be positive when the total wear rate due to erosion-corrosion is higher than the sum of the wear rates due to pure erosion and flow corrosion. Negative synergy (antagonism) is expressed if this difference is lower. Synergy comprises the following components:

$$S = \Delta C + \Delta E \tag{2.29}$$

where ΔC is the erosion enhanced corrosion rate and ΔE is the corrosion enhanced erosion rate. Wood and Hutton [55, 56] who performed a study on synergistic trends in published results which included cavitation erosion and slurry erosion, found that synergy could be categorised into two groups, namely medium synergy and high synergy. A best fit line expressed by Eq. (2.30) and (2.31) were obtained for these groups:

Medium synergy group

$$\frac{S}{C} = exp\left[1.277\, ln\left(\frac{E}{C}\right) - 1.9125\right] \tag{2.30}$$

High Synergy group

$$\frac{S}{C} = exp\left[0.755\, ln\left(\frac{E}{C}\right) + 1.222\right] \tag{2.31}$$

For the medium synergy group, a synergistic effect of approximately 30 percent was found, while for the high synergy group, a synergy of more than 60 percent was reported. A

magnification factor (M_f) defined as the ratio of the total erosion-corrosion rate divided by the sum of pure erosion and flow corrosion as shown in Eq. (2.32) was also introduced:

$$M_f = \frac{T}{E + C} \tag{2.32}$$

The magnification factor is useful in understanding the additional wear rate due to erosion-corrosion, where a ratio of less than 1 would mean negative synergy is present whereas positive synergy is present if this ratio is more than 1.

Other investigators have used different terms to express the interaction between erosion-corrosion. Another relationship used to express erosion-corrosion interaction is shown in Eq. (2.33) [57-59]:

$$K_{ec} = K_{co} + K_{eo} + \Delta K_e + \Delta K_c \tag{2.33}$$

where K_{ec} is the total erosion-corrosion rate, K_{co} is the corrosion rate in the absence of erosion, ΔK_c is the effect of erosion on corrosion , K_{eo} is the erosion rate in the absence of corrosion and ΔK_e is the effect of corrosion on erosion [57-59]. Essentially, the fundamental definition of Eq. (2.33) is similar to Eq. (2.27) and (2.29), but the only difference is the terms used by different investigators. Section 2.3.3 and 2.3.4 will review in more detail the synergistic effects and interaction between erosion enhanced corrosion *(ΔC)* and corrosion enhanced erosion *(ΔE)*.

2.3.3 Erosion enhanced corrosion (ΔC)

Stack *et al*. [57] developed an erosion-corrosion map with the aim of identifying the transition between erosion-corrosion regimes using a rotating cylinder electrode apparatus. They found that the passive current density increased with increasing velocity in the presence of erodents and at a minimum velocity of 2 m s^{-1}, the presence of particles did not cause any effect on the passive current. Only after the velocity was increased to 4 m s^{-1} did the passive current increase, indicating the passive film was being destroyed and repaired continuously.

Aiming *et al*. [60] who conducted erosion-corrosion tests on stainless steel in wet phosphoric acid (pH = 1) and gypsum using a slurry impeller apparatus, found that there was also a critical velocity of 12 m s^{-1} where the corrosion rate increased. This was attributed to the surface passive layer being removed at high velocities. Another important observation from their experiment was that the corrosion and erosion-corrosion wear rates increased with an increase in temperature from 40 °C to 80 °C. According to them, erosion can enhance corrosion by removing the passive film and exposing the metal surface to the corrosive medium. If the metal is unable to repassivate fast enough, then there will be significant corrosion. This explanation has also been provided by other authors [56, 61-66].

As discussed in section 2.2.2, the mass transfer coefficient varies with flow rate and affects corrosion rates. Erosion can increase the mass transfer coefficient by a number of methods [67]. The first mechanism is through the removal of corrosion products on the surface of the material. Erosion also has the effect of increasing the turbulence intensity when particles interact with the boundary layer. Another mechanism in which erosion can increase the mass transfer coefficient is by roughening the surface, leading to an increased electrochemical activity as it allows localised corrosion to take place. This occurs due to the formation of micro-galvanic cells on the surface promoting the coupling between the anodic and cathodic sites at a micro and/or nano level which causes localised corrosion.

Pitting has been observed by many investigators during erosion-corrosion [68-72]. In studying the initiation of corrosion pits by slurry erosion on stainless steel, Burstein and Sasaki [71] found that below a pitting potential, slurry erosion causes formation of more metastable pits compared to non-erosive conditions. This was believed to be due to the continuous rupture and removal of the passive film by solid particle impacts. The higher the number of impacting particles, the higher the number of metastable pits formed, leading to a higher probability of reaching stable pits.

2.3.4 Corrosion enhanced erosion (ΔE)

Li *et al*. [54] proposed a mechanism for corrosion enhanced erosion. A jet impingement rig was used to erode aluminium in aqueous slurry and it was identified that detachment of metallic flakes was the main wear mechanism during erosion-corrosion. It was observed that the flakes tend to be removed by cracking in fragments after multiple erodent impacts, unlike pure erosion, where the flakes were removed by ductile fracture. It was concluded that corrosion enhances erosion by localised attack at sites where the passive

layer is ruptured during impact. This localised corrosion phenomenon initiates cracks at the root of the flakes and propagates with particle impacts, making the flakes vulnerable to detachment. This leads to an enhanced erosion rate.

In addition to the suggested mechanisms provided for the effect of corrosion on erosion, Aiming *et al*. [60] also provided several mechanisms for corrosion enhanced erosion. The first proposed mechanism was due to the fact that corrosion normally starts at grain boundaries. Neville *et al*. [73] and Toro *et al*. [74] have observed this phenomenon experimentally. Neville *et al*. [73] who performed erosion-corrosion tests on grey cast iron, noticed that there were corrosive attacks at the graphite/matrix interface. It was proposed that this would cause loosening of intermediate grains of metals and subsequent removal by particle impact. Toro *et al*. [74] also suggested intergranular corrosion as a mechanism for material removal of the metallic matrix for the unnitrided stainless steel specimens.

The second mechanism suggested by Aiming *et al*. [60] is that the degradation of the mechanical properties of the metal due to corrosion reduces its wear resistance, making it more susceptible to erosion. However, no details were provided on which mechanical property might be affected by corrosion. Matsumura *et al*. [75] suggested another possible mechanism on how corrosion can enhance erosion. As the particle impacts the passive film and damages it, dissolution of the surface leads to the elimination of the work hardened layer and increases the surface roughness. This effect could cause enhanced erosion rates as now the particle is able to penetrate deeper into the surface. Wood and Hutton [55,76] as well as Wang and Stack [77] have also provided an excellent review on the interactions between erosion, corrosion and critical parameters influencing erosion-corrosion.

2.3.5 Erosion-corrosion test rigs

In order to determine the total wear rate caused by the combined effect of erosion and corrosion, various rigs have been designed to measure this effect. This section will review the working principles of some of the commonly used rigs and discuss the advantages and disadvantages of these rigs.

2.3.5.1 Slurry pot erosion tester

The slurry pot erosion tester [18, 19 and 22] which is normally used for erosion testing can also be used for erosion-corrosion experiments by changing the slurry medium to a corrosive slurry. Cylindrical specimens are placed on a specimen holder at the end of the shaft which is rotated in a slurry pot using a motor. The motor is connected to the shaft through a toothed belt and a pulley. The speed of the motor is controlled by adjusting the frequency of the variable speed drive. The advantage of using a slurry pot is that the slurry and erodent which are contained within the pot can be handled easily. This rig also produces repeatable and reproducible results with low errors. The disadvantage of using this rig is that the impact angles of the erodent cannot be controlled due to the rotating flow field of the slurry. The cylindrical sample geometry also makes polishing of the test sample difficult. A more detailed explanation on this test rig which is used in this work is given in Section 3.3.2. There are also other designs of the slurry pot used by other researchers [20, 66]. However, the basic principle of the rig remains the same, where the sample is placed in a pot while being eroded by a rotating flow field.

2.3.5.2 Jet impingement rig

The jet impingement apparatus shown in Figure 2.21 is one of the various rigs used to simulate erosion-corrosion conditions in a controlled laboratory environment [27, 78, 79]. The rig consists of a large reservoir tank to store electrolyte which is pumped through an ejector to the specimen [80]. The erodent is introduced into the system by allowing the pressure drop across the nozzle (which creates a region of low pressure) to lift the sand to the ejector. Electrochemical measurements can be made by placing the counter and reference electrode just before the nozzle and connecting them to the working electrode which in this case is the specimen itself [80]. The advantage of this rig is that the velocity and the impact angle of the erodent can be controlled by adjusting the nozzle and sample holder angle respectively. The disadvantage of using this rig is that the sand concentration can be inconsistent if the suction tube is blocked with erodents as it relies entirely on Bernoulli's effect. A similar technique has also been used by other experimenters [54, 62].

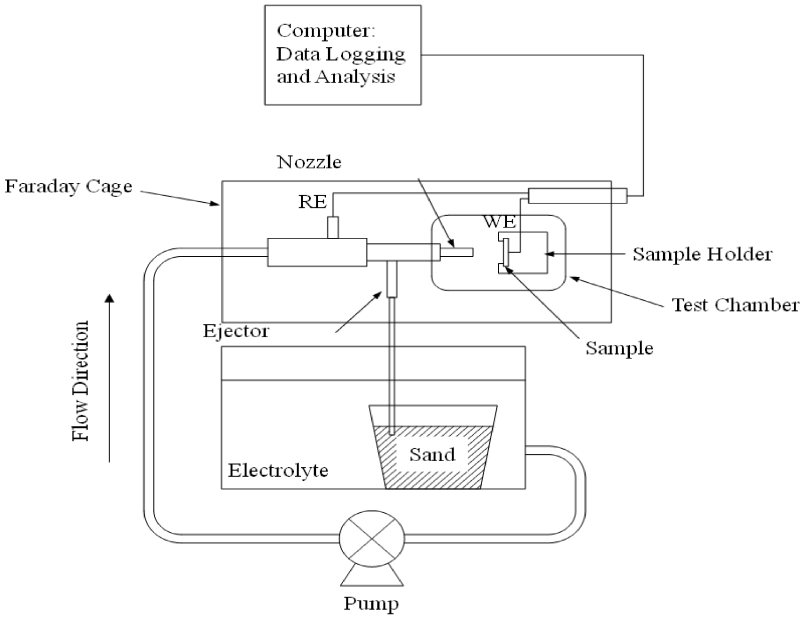

Figure 2.21 Schematic of a jet impingement rig [80]

2.3.5.3 Coriolis erosion tester

The coriolis erosion tester shown in Figure 2.22 [81-83], uses a combination of centrifugal and coriolis acceleration in a rotating rotor to pass slurry across the test surface. This causes the erodent to move against the surface and cause wear erosion. It consists of a rotor which fits two specimen holders on either side. Erodent is channelled from the slurry inlet pot from the central chamber outwards as the rotor is rotated. The erodent impinges against the test surface as a result of coriolis acceleration. The advantage of using a coriolis erosion tester is that the mixture of elastic and plastic deformation that occurs during the test simulates industrial equipments quite well. The disadvantage with this rig design is that the contact mode depends on the slurry concentration. When the slurry is concentrated, particle rebounding is limited by particle interaction and many particles slide along the specimen surface [82]. This rig is dominated by erosion at low impact angles.

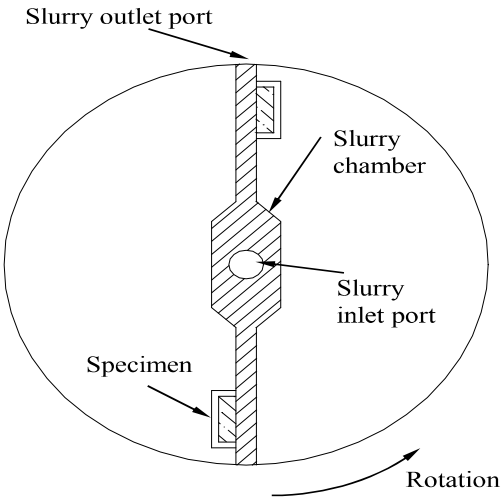

Figure 2.22 Schematic of a coriolis erosion tester [83]

2.3.5.4 Pipe flow loop

Erosion–corrosion is a serious problem in pipelines transporting slurries. Laboratory simulations of erosion-corrosion tests often do not reflect the reality of erosion-corrosion that occurs in pipelines. In order to overcome this problem, some investigators have conducted experiments on pipe flow loops [84, 85]. Although most of the pipe flow loops are often scaled down to laboratory sizes, the flow field can still be predicted in an accurate manner. Using a pipe flow loop, erosion-corrosion effects on actual geometries of pipe bends, tees, and elbows could be investigated. Flow loops consist of a stirrer slurry tank where the slurry is stirred and acts as a reservoir to store the slurry [84, 85]. The slurry is then pumped from the tank to the loop and recirculated back to the tank. Besides being able to predict erosion-corrosion on actual pipe geometries, the pipe flow loop can also use actual pipe thickness to calculate the eroding rate. Electrochemical measurements can be done randomly at points of interest along the pipe. This type of experimental technique is rarely used due to the high cost of construction, maintenance and due to space limitation within a laboratory.

2.3.5.5 Rotating cylinder

Another rig which has been used to study erosion-corrosion is the rotating cylinder electrode [86-89]. This rig consists of an inner cylinder which is mounted on an enclosed shaft. A platinum electrode used as the counter electrode is mounted against the inside wall

of the vessel to provide a hydrodynamically smooth surface [87]. The working electrode is placed in the middle of the inner rotating cylinder, while the reference electrode is placed on a side arm outside the test cell, connected to the system by an electrolyte bridge. The advantage of this rig is that it is easy to operate and construct. Besides that, the rotating cylinder electrode with its well characterised hydrodynamics can be used to study the effect of solid particle erosion on the mass transfer process [89]. On the other hand, the disadvantage of this rig is that similar to the slurry pot, the impact angles cannot be controlled due to its rotational flow field. Figure 2.23 shows a schematic of the rotating cylinder apparatus.

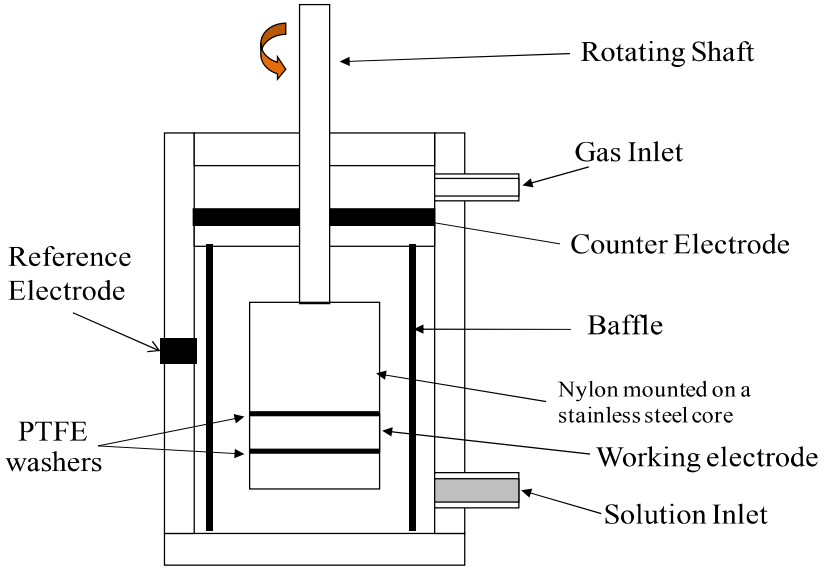

Figure 2.23 Schematic of a rotating cylinder [86]

~~*2.4 Stainless Steels*~~

~~*2.4.1 Introduction*~~

~~Stainless steels are defined by ASM International as iron based alloys that contain a minimum of 11% chromium, which allows it to be corrosion resistant in the atmosphere [90]. The corrosion resistance of stainless steel is achieved through the formation of a thin chromium oxide film layer on the surface of the metal which inhibits corrosion [91]. Stainless steels can be divided into five types namely martensitic, ferritic, austenitic, duplex (combination of austenitic plus ferritic) and precipitation-hardenable alloys. The images of the microstructures of the first four groups are shown in Figure 2.24 (a) (d) [97].~~